Energy materials

Mesopore-dominated N, S co-doped carbon as advanced oxygen reduction reaction electrocatalysts for Zn-air battery

Shouting Wang[1], Ye Chen[1], Yaling Zhao[2], Gangya Wei[2], Dongliang Li[1,*], and Xupo Liu[1,*]

[1] *School of Materials Science and Engineering, Henan Normal University, Xinxiang 453007, Henan, People's Republic of China*
[2] *School of Chemistry and Chemical Engineering, Henan Normal University, Xinxiang 453007, Henan, People's Republic of China*

ABSTRACT

Oxygen reduction reaction (ORR) is a crucial step for Zn-air batteries (ZABs), which requires low-cost yet efficient catalysts to satisfy the practical application. Heteroatom-doped, especially N, S-doped carbon, has attracted intensive attention as promising ORR catalysts. However, the issues of devitalized micropore channels covered by reaction intermediates and unstable configuration of N, S heteroatoms obtained by post-doping treatment have largely hindered the development of carbon-based catalysts. Herein, mesopore-dominated N, S co-doped hierarchical carbon has been constructed by the hard-soft (SiO_2–$ZnCl_2$) template strategy based on waste biomass. The optimal catalyst (NSC-PT-0.1) exhibits a mesopore-dominated hierarchical porous structure with high S_{BET} (2357.55 $m^2\ g^{-1}$) and N, S content ($\sim$ 2.32 at.%), resulting in comparable ORR activity in acid ($E_{1/2}$ = 0.69 V) and alkaline ($E_{1/2}$ = 0.83 V) media to Pt/C. Moreover, different biomass precursors of Carrot, Whorled stonecrop, and Ginkgo leaf have been explored to verify the generality of hard-soft template strategy. When NSC-PT-0.1 is applied as the air electrode, the assembled ZAB exhibits high power density of 155.55 $mW\ cm^{-2}$ and long-term cycling stability over 216 h. Therefore, this work provides a versatile hard-soft template strategy to synthesize efficient ORR catalysts for ZABs application through the resource utilization of biomass.
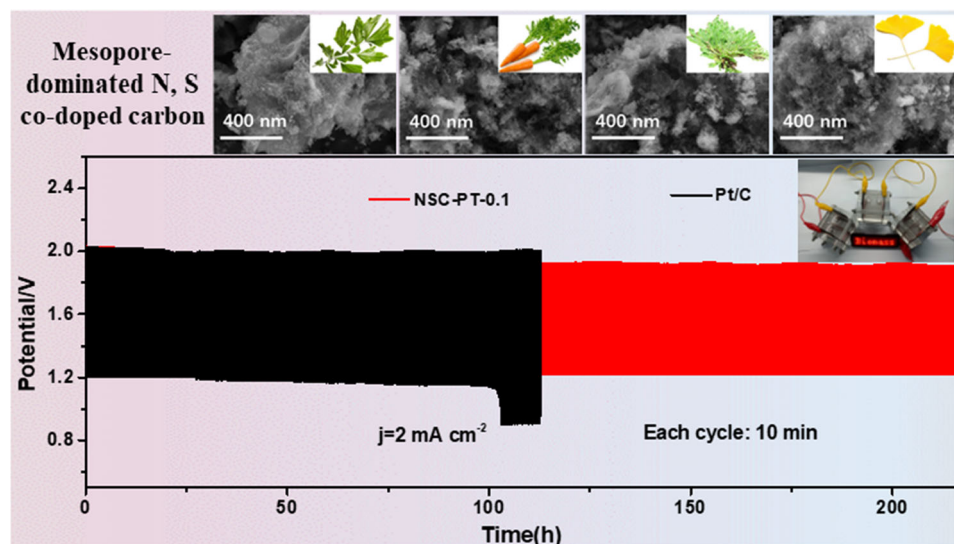
Ⓐ Springer

GRAPHICAL ABSTRACT

Mesopore-dominated N, S co-doped carbon is synthesized by one-step pyrolysis of waste biomass and SiO$_2$–ZnCl$_2$ hard-soft templates. The optimal catalyst exhibits excellent ORR performances in alkaline and acid media as well as promising Zn-air battery application.

Introduction

Zn-air batteries (ZABs) are considered as one of the most viable options to next-generation energy storage system because of their high theoretical energy density (1086 W·h/Kg) and low cost [1–3]. To achieve the high performance of ZABs, the noble metal catalysts (such as Pt-based catalysts) are often used for accelerating the slow oxygen reduction reaction (ORR) at air electrode [4, 5]. Recently, heteroatom-doped (N, S, B, P, etc.) metal-free carbon catalysts have been generally considered as the most promising alternatives to replace the air electrode of noble metal Pt-based catalysts, which resolves the scarcity and expensive bottlenecks [6, 7].

Heteroatom doping, such as N, S, etc., can manipulate the absorption of O$_2$ and improve ORR kinetics through the redistribution of charge density of adjacent C atoms. Nevertheless, the current study of heteroatom-doped carbon suffers from low doping contents and unstable configuration of heteroatoms

obtained by the post-doping. It is of great significance to select low-cost, natural treasure-waste biomass as carbon precursor and N, S sources, to achieve heteroatom self-doping [8–12]. Additionally, the discrete distribution of active sites in the N, S co-doped carbon catalysts brings the requirement of hierarchically porous structure, which ensures an efficient mass transfer [13, 14]. Templates are commonly employed to regulate the porosity, including acid oxidation (H$_3$PO$_4$, HNO$_3$, H$_2$O$_2$, etc.) [15], alkali oxidation (KOH, NaOH, etc.) [16], and metal salt activation (ZnCl$_2$, KCH$_3$COO, NaNH$_2$, KHCO$_3$, etc.) [3, 17–21]. However, the active sites in the micropore channels formed by a single template to prepare biomass-derived carbon materials would be covered by other reaction intermediates and eventually lead to rapid deactivation [5, 22, 23]. Therefore, the hard-soft template (SiO$_2$-ZnCl$_2$) strategy is employed to satisfy accessible catalytically active sites, shorten the diffusion pathways of reactants and products, and increase the specific surface area [20, 24–30]. On the basis of the covered active sites and the

unstable configuration of heteroatoms, the waste biomass is applied as carbon precursors and heteroatoms sources to realize heteroatoms self-doping; meanwhile, the hard-soft template strategy is employed to optimize pore structure features.

Hence, N, S co-doped porous carbon materials have been synthesized by annealing the mixtures of Pointed tail leaf (carbon precursor and N, S sources) and templates (SiO_2-$ZnCl_2$) through the hard-soft template approach. The as-prepared material has the unique mesopore-dominated hierarchical porous structure, high specific surface area, and high N, S doping content. The optimal catalyst (NSC-PT-0.1) exhibits a comparable ORR electrocatalytic activity with acid resistance ($E_{1/2}$ = 0.69 V) and basic resistance ($E_{1/2}$ = 0.82 V), while the stability and methanol resistance are superior to Pt/C. Furthermore, the assembled ZAB using NSC-PT-0.1 as air electrode reveals a higher peak power density of 155.55 mW cm^{-2} and better cyclic stability (216 h) than Pt/C-based ZAB. Inspired by above performance, we have prepared many other mesopore-dominated hierarchical heteroatom-doped carbon materials by pyrolysis of the mixture of waste biomasses (Carrot, Whorled stonecrop, and Ginkgo leaf) and the optimal template dosages. This study not only develops a promising hard-soft template strategy for preparing economical and efficient catalysts for ZABs but also provides attractive solutions tackling green technology challenges of severe environmental issues and energy crises.

Experimental section

Materials

Silica (SiO_2, ~ 30 nm), zinc chloride ($ZnCl_2$, 98%), potassium hydroxide (KOH, 85%), zinc acetate ($Zn(Ac)_2$, AR), sulfuric acid (H_2SO_4, 98%), hydrofluoric acid (HF, 40%), isopropyl alcohol ((CH_3)$_2$CHOH, AR), and polytetrafluoroethylene (PTFE, 60 wt%) were purchased from Aladdin Reagent Co., Ltd. Commercial Pt/C (20 wt%) electrocatalyst and Nafion solution (5 wt%) were provided by Shanghai Hesen Electric Co., Ltd. Four kinds of natural waste biomass (the leaf of Pointed tail, Carrot, Whorled stonecrop, and Ginkgo) were purchased from a vegetable market in Xinxiang and washed for further

application. All the chemicals were used directly without further purification.

Preparation of N, S co-doped hierarchically porous carbon materials

The dried power of Pointed tail leaf (1 g) and SiO_2 (x g, x = 0.04, 0.07, 0.1, 0.5, and 1 g, respectively) was firstly mixed and thoroughly ground with $ZnCl_2$ (0.682 g) in an agate mortar for 30 min. The precursors were pyrolyzed in a tube furnace in N_2 gas flow at 300 °C for 2 h and continuously heated to 900 °C for 2 h. Subsequently, the pyrolyzed product was etched with 15% HF solution for 24 h to remove the hard templates (SiO_2) and other impurities from the pyrolysis of soft templates ($ZnCl_2$). Finally, the product was washed with a large amount of deionized water, filtered, and placed in a blast drying oven at 80 °C for 12 h, to obtain N, S co-doped porous carbon materials named NSC-PT-x. Two control samples, NSC-PT-Z ($ZnCl_2$) and NSC-PT–S (SiO_2), were synthesized following the same procedure.

To exploit the universality of soft-hard templates, the Carrot (i.e., CL), Whorled stonecrop (i.e., WS), and Ginkgo leaf (i.e., GL) were employed as carbon precursors and N, S sources to achieve the N, S co-doped hierarchically porous carbon catalysts. The optimal hard-soft templates were employed to synthesize the catalysts, which are donated as NSC-CL-0.1, NSC-WS-0.1, and NSC-GL-0.1. Meanwhile, the control samples without templates were also obtained, which were named as NSC-CL-0, NSC-WS-0, and NSC-GL-0, respectively.

Characterization

Microscopic surface morphology and crystal structure of the synthesized materials were characterized by the field emission scanning electron microscope (FE-SEM) and transmission electron microscope (TEM) on Hitachi High-Technologies Corporation SU8010 and JEOL JEM-2100. The crystal phases of materials were identified by X-ray diffraction (XRD) patterns on the Bruker-D8 instrument with Cu-Kα radiation. Raman spectra were measured directly on LabRAM HR Evolution with 532-nm excitation laser to study the degree of defects. A thermogravimetric analysis/differential thermal analysis (TG/DTA) thermal analyzer (NETZSCH STA449F3) was used for testing weight losses in N_2 atmosphere up to

1000 °C. The Brunauer–Emmett–Teller (BET) surface area and pore size distribution were analyzed by N_2 adsorption–desorption isotherms on the Quantachrome Autosorb Station iQ2 instrument. X-ray photoelectron spectroscopy (XPS) was used to characterize the surface chemical state analysis of samples on Thermo Scientific ESCALAB250. The contact wettability was measured by the water contact angle test on KRüSS DSA25.

Electrochemical testing of ORR

All electrochemical experiments were carried out on an electrochemical workstation (CHI660E) with a three-electrode system. Hg/HgO electrode and saturated calomel electrode were regarded as the reference electrodes in 0.1 M KOH and 0.5 M H_2SO_4, Pt foil (1 cm^2) electrode as the counter electrode, and catalyst-coated glassy carbon electrode (GCE, $d = 3$ mm or 5.61 mm) as the working electrode, respectively. The electrolytes were N_2/O_2-saturated 0.1 M KOH or 0.5 M H_2SO_4.

Preparation of working electrode: 100 μL Nafion solution (5 wt.%) and 4.9 mL ultrapure water were dispersed in a 5-mL sample tube to obtain 0.1 wt% Nafion solution. 1 mg catalyst and 60 μL 0.1 wt% Nafion solution were ultrasonically dispersed for 30 min to obtain the uniform catalyst ink. Subsequently, 6/18 μL catalyst ink was loaded on a clean glassy carbon electrode (GCE, $d = 3/5.61$ mm) to acquire the working electrode for cyclic voltammetry (CV) and linear sweep voltammetry (LSV) technologies. Besides, the Pt/C electrode was also prepared using the same method.

ORR tests: A certain amount of 0.1 M KOH or 0.5 M H_2SO_4 electrolyte was added into a five-port electrolytic cell, and a constant flow of N_2 or O_2 was introduced to the solution to saturation. Electrode activation was performed by CV technique and tested at scan rates of 10 mV s^{-1} with potential intervals of 0.07 $\sim$ 1.17 V (0.1 M KOH) or 0.17–1.27 V (0.5 M H_2SO_4), respectively. The electrochemical active surface area (ECSA) of the catalysts was evaluated by measuring the double-layer capacitance (C_{dl}) with different scan rates (5, 10, 15, 20, 30, 40, and 50 mV s^{-1}). The accelerated stability tests and methanol tolerance experiments were carried out by

the CV curves. The scanning speed of the LSV curve was 10 mV s^{-1}, the potential interval was the same as that of CV test, and the rotation speed was 1600 rpm. All potentials were recorded and converted to the potential versus RHE based on the equations of $E_{(RHE)} = E_{(Hg/HgO)} + 0.0591$ pH + 0.098 V (pH = 13 for 0.1 M KOH) and $E_{(RHE)} = E_{(SCE)} + 0.0591$ pH + 0.24 V (pH = 0 for 0.5 M H_2SO_4).

The hydrogen peroxide yield ($H_2O_2\%$) and the number of electron transfers (n) of catalysts were calculated according to the following equations:

$$n = \frac{4I_d}{I_r/N + I_d} \tag{1}$$

$$H_2O_2 = \frac{2I_r/N}{I_r/N + I_d} \times 100\% \tag{2}$$

where I_d is the disk current, I_r refers to the ring current, and N is the current collection efficiency of the Pt ring ($N = 0.37$).

Assembly and performance test of Zn-air batteries

Assembly of Zn-air batteries: 3 mg catalyst, 200 μL $(CH_3)_2CHOH$ solution, 16 μL 5 wt% Nafion solution, and 8 μL 5 wt% PTFE were mixed and ultrasonically treated for 30 min to obtain uniformly dispersed catalyst ink. The catalyst ink was loaded on carbon paper with the loading of 2 mg cm^{-2} and dried naturally. The air electrode was also prepared by the same process using the commercial Pt/C catalyst. The ZAB was assembled with the catalyst-coated carbon paper as the air cathode, a polished Zn foil (0.2 mm) as the anode, and 6.0 M KOH containing 0.2 M $Zn(Ac)_2$ solution as the electrolyte.

Performance test of Zn-air battery: The charge–discharge polarization curves were performed by LSV at a scan rate of 5 mV s^{-1}. The galvanostatic discharge curves were tested by chronopotentiometry (CP) technology at different galvanostatic current densities (1, 2, 5, 10, 20, 50, and 100 mA cm^{-2}). In addition, the cycling stability was detected by using the CP technique at 2 mA cm^{-2} with a cycling interval of 10 min (5 min for charging and 5 min for discharging).

Scheme 1 Schematic illustration of synthetic process for NSC-PT, NSC-CL, NSC-WS, and NSC-GL series of catalysts.
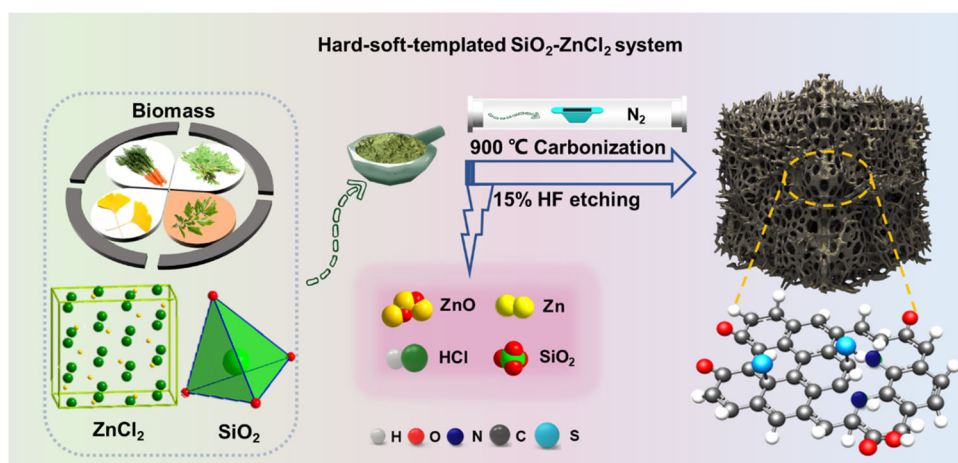
Results and discussion

Morphology and composition characterization

The mesopore-dominated N, S co-doped hierarchical porous carbon materials have been synthesized by the hard-soft template strategy, as shown in Scheme 1. The morphologies of NSC-PT series of catalysts were characterized by SEM. Figure 1a reveals a disorderly stacked fragmentary structure of NSC-PT-0. With the increased amounts of hard template SiO_2 from 0.04 to 0.1 g, porous structures are gradually generated (Fig. S1a–b and Fig. 2b). Such condition of 0.1 g SiO_2 under the presence of $ZnCl_2$ soft template can provide hierarchically porous structure (Fig. 1b). Subsequently, with the hard template dosage continuously increasing from 0.5 to 1 g, more macropores are formed (Fig. S1c, d). When a single soft template or hard template is introduced, the surface morphology of NSC-PT-Z (Fig. 1c) and NSC-PT–S (Fig. 1d) becomes fluffy and porous
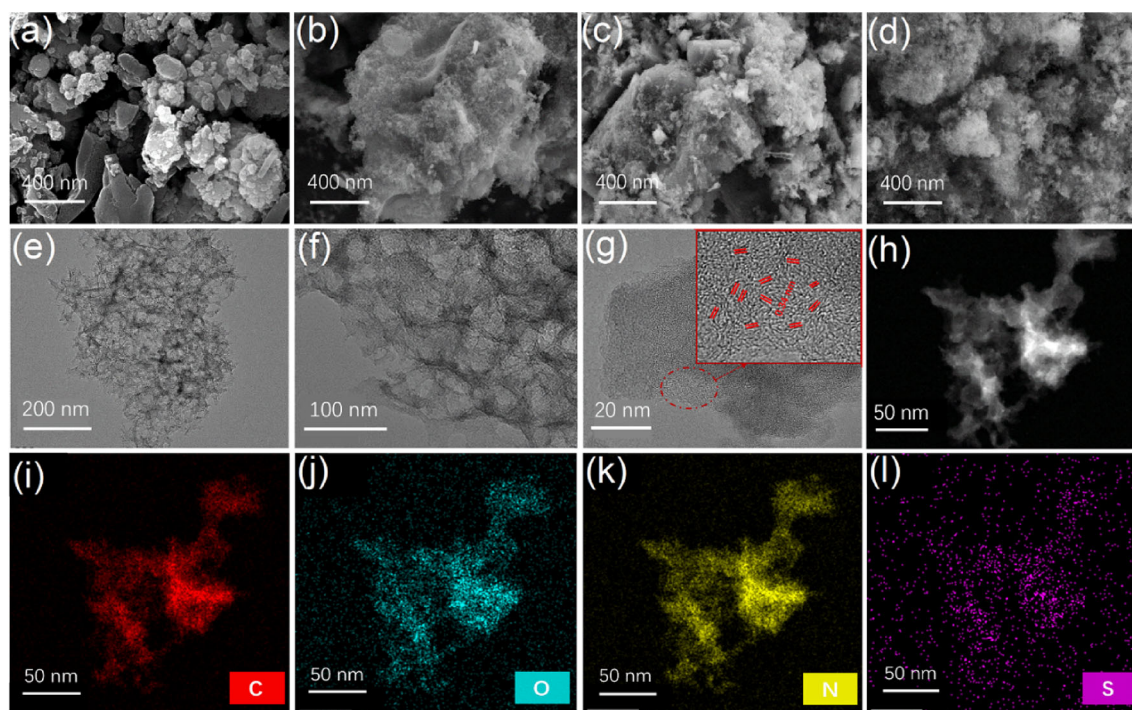

Figure 1 SEM images of NSC-PT-0 (**a**), NSC-PT-0.1 (**b**), NSC-PT-Z (**c**), and NSC-PT–S (**d**); TEM (**e**–**f**), HR-TEM (**g**), HR-TEM and element scanning images of NSC-PT-0.1 (**h**–**l**).
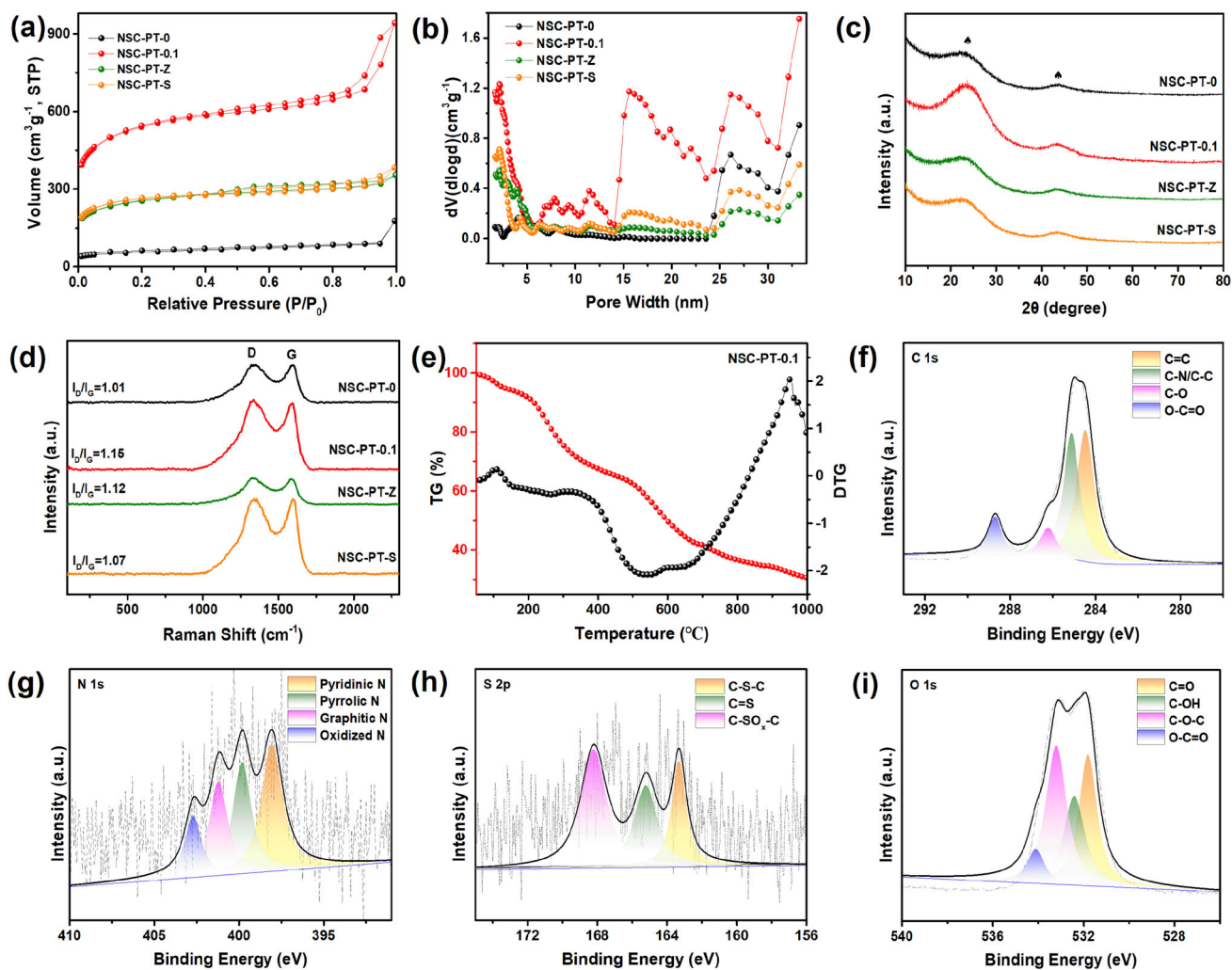
Figure 2 N$_2$ adsorption/desorption isotherms (**a**), pore size distribution curves (**b**), XRD patterns (**c**), and Raman spectra (**d**) images of NSC-PT-x, NSC-PT-Z, and NSC-PT-S; TGA curves (**e**), high-resolution C 1s (**f**), N 1s (**g**), S 2p (**h**), and O 1s XPS spectra of NSC-PT-0.1 (**i**).

[31, 32]. The as-prepared NSC-PT-0.1 catalyst with two templating agents, possesses the rich mesoporous morphology of the SiO$_2$ template. More detailed porosity information will be discussed in following BET data. TEM characterization analysis is applied to further study the morphology and structure of the catalysts. The mesopore-dominated porous structure can be found of the NSC-PT-0.1 catalyst in Fig. 1e, f. The HR-TEM image of NSC-PT-0.1 is further observed (Fig. 1g), and the edge of the material shows a large number of discrete lattice fringes with lattice spacings of about 0.34 nm, which correspond to the (002) crystal planes of graphitized carbon [33, 34]. The result indicates that the NSC-PT-0.1 undergoes partial graphitization after high-temperature pyrolysis, which can facilitate the transport

of electrons [35]. According to the HR-TEM and element surface scan images (Fig. 1i–l), the elements of C, O, N, and S are uniformly distributed along with the structure of mesopore-dominated carbon, implying the successful preparation of hierarchically nanostructured carbon materials.

The influence of template dosages on pore structure and specific surface area of NSC-PT-x has been investigated. Although all carbon materials show type-IV N$_2$ adsorption/desorption isotherms, the porosity changes with the amount of template agent (Fig. 2a, b, Fig. S2a, b, and Table S1). NSC-PT-0 is obtained by carboning the pure Pointed tail leaf without the hard-soft template, whose specific surface area (S$_{BET}$) is 247.35 m^2 g^{-1}, corresponding to the rough topography of the SEM image. As the hard

template dosage increases, the determined S_{BET} values firstly increase and then decrease, and the NSC-PT-0.1 shows the largest S_{BET} of 2357.55 $m^2\ g^{-1}$. Meanwhile, the $d_{Average}$ values are mainly distributed in the range from 3.0 to 8.5 nm, proving the successful synthesis of mesopore-dominated porous carbon materials. In addition, without the introduction of the template, the specific surface area (S_{BET}) of NSC-PT-0 is just 247.35 $m^2\ g^{-1}$. As just a single soft template or hard template is added, the S_{BET} (1095.55 and 1128.51 $m^2\ g^{-1}$) of the catalyst increases significantly. Notably, when hard-soft templating agents are both added, the S_{BET} (2357.55 $m^2\ g^{-1}$) of the catalyst is almost double that of adding only one single templating agent. Besides, two broad diffraction peaks around 23° and 44° in the XRD patterns of all catalysts represent the (002) and (101) planes of graphitized carbon in Fig. S2c and Fig. 2c, respectively [36]. The wider diffraction peak (002) of NSC-PT-0.1 indicates that the (002) crystal plane peak is weakened more obviously, meaning higher defectivity [37]. Besides, the D-band corresponds to disorder and defects in the graphite crystal lattice, whereas the G-band reflects crystalline ordering of the graphitic basal-plane. The I_D/I_G value of NSC-PT-0.1 (1.15) is larger than other catalysts (Fig. 2d, Fig. S2c, d, and Table S1), indicating more defects are generated, corresponding to XRD results.

Thermogravimetric analysis (TGA, Fig. 2e) of NSC-PT-0.1 in the N_2 atmosphere was performed to further explore the pore formation mechanism of carbon materials. The high-temperature pyrolysis reaction is mainly divided into three stages: (i) 25–267 °C, the evaporation of free and bound water on the surface occurs; meanwhile, the soft templates of $ZnCl_2$ molecules enter the carbon frameworks and react with water molecules to produce ZnO (formula (1)) [31]. (ii) 267–538 °C, the weight loss at this stage is mainly attributed to the decomposition of cellulose, hemicellulose, and lignin in the waste biomass [38]. (iii) 538–900 °C, the reduction of ZnO in carbon frameworks happens to obtain metallic Zn and CO/CO_2 (formula (2)) [39]. After reaching the boiling point of Zn ($\sim$ 900 °C), the Zn elements turn into a gaseous state and leave the carbon skeletons [40]. Based on the above reactions, the formation mechanism of pore structure of NSC-PT-0.1 was speculated during the pyrolysis. The evaporation of water and the escape of Zn vapor from the surface mainly provide the microporous structure, whereas the

mesoporous structure is fabricated by ZnO in the carbon frameworks and the hard template of SiO_2. The gas molecules (CO/CO_2) in the molten carbon frameworks also easily rupture to form a meso/microporous structure [41]. The mesopore-dominated hierarchically porous structure not only facilitates the diffusion of oxygen molecules and exposes more catalytically active sites, but also effectively promotes the permeation process of electrolytes in active materials.

$$ZnCl_2 + H_2O \ \rightarrow \ ZnO + HCl \tag{3}$$

$$ZnO + C \ \rightarrow \ CO/CO_2 + Zn \tag{4}$$
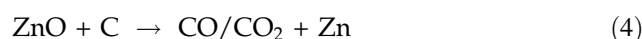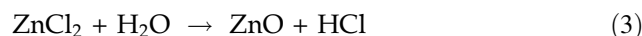
The full XPS spectra contain C, N, O, and S elements are detected (Fig. S3a), matching well with the uniform elemental distribution in the HR-TEM image. Four component peaks of C 1 s spectrum with binding energies at $\sim$ 284.5 eV, $\sim$ 285.1 eV, $\sim$ 286.2 eV, and $\sim$ 288.7 eV, correspond to C=C, C−N/C−C, C−O, and O−C=O species (Fig. 2f). Figure 2g shows that the N 1 s high-resolution spectrum can be fitted to four positions at $\sim$ 398.1 eV (pyridinic-N), $\sim$ 399.8 eV (pyrrolic-N), $\sim$ 401.2 eV (graphitic-N), and $\sim$ 402.7 eV (oxidized-N). Among them, pyridinic-N and graphitic-N with suitable electronegativity and electron configuration have been confirmed to provide catalytically active centers for ORR [42]. The high-resolution spectrum of S 2p can be divided into three peaks (Fig. 2h), C−S−C ($\sim$ 163.3 eV), C=S ($\sim$ 165.2 eV), and C−SO$_x$−C ($\sim$ 168.2 eV). Doping of N, S heteroatoms changes the valence states of adjacent carbon atoms in the carbon frameworks, thereby improving ORR electrocatalytic activity [43]. Finally, the high-resolution spectrum of the O element is fitted and analyzed (Fig. 2i). It can be seen that the peaks with different intensities appear at $\sim$ 531.8 eV, $\sim$ 532.4 eV, $\sim$ 533.2 eV, and $\sim$ 534.1 eV, corresponding to C=O, C−OH, C−O−C, and O−C=O groups [44]. Due to the electronegativity difference between carbon and heteroatoms (δ_C = 2.55, δ_N = 3.04, and δ_S = 2.58), the carbon-heteroatom bond is easily polarized and induces positive/negative charges on adjacent carbon atoms, which is conducive to oxygen adsorption and reduction [45–47]. In detail, the surrounding carbon atoms are positively charged due to the appearance of the above oxygen-containing functional groups, which can adsorb OH$^-$ or H_2O through electrostatic attraction. It can effectively

improve the electron transfer between the material surface and reaction intermediates, thereby enhancing the ORR catalytic activity [48]. In addition, the hydrophilic groups can improve the hydrophilicity of carbon materials by utilizing the interaction between hydrogen bonds and water molecules. The water contact angle of NSC-PT-0.1 is determined to be 3° (Fig. S3b), indicating that the material has super hydrophilicity. The hydrophilicity promotes the efficient transport of mass/ions and improves the electrocatalytic activity of the materials.

Electrocatalytic performance

The electrocatalytic performance of the as-prepared catalysts was evaluated in alkaline and acidic media using a three-electrode system. The ORR performance at alkaline condition was firstly investigated. The CV curves, of NSC-PT-x with different ratios of the hard-soft templates, are tested in 0.1 M KOH saturated with N_2, which reveals a rectangular-like appearance without cathodic oxygen reduction peaks in Fig. S4a. However, in the O_2-saturated electrolyte, the CV curves immediately exhibit an obvious cathodic peak, suggesting that all the catalysts have electrochemical reduction ability to oxygen. It is observed that the optimal ORR activity is achieved for NSC-PT-0.1 ($E_s = 0.84$ V). In order to evaluate the kinetics mechanism of electrocatalysts toward ORR, the LSV plots were obtained by the specific rotating ring disk electrode (RRDE) from Pine company. As depicted in Fig. S4b, c and Table S2, NSC-PT-0.1 possesses an exceptional half-wave potential of 0.83 V with an onset potential of 0.93 V, better than those of NSC-PT-0.04 ($E_{1/2} = 0.77$ V, $E_{onset} = 0.89$ V), NSC-PT-0.07 ($E_{1/2} = 0.80$ V, $E_{onset} = 0.90$ V), NSC-PT-0.5 ($E_{1/2} = 0.79$ V, $E_{onset} = 0.90$ V), and NSC-PT-1 ($E_{1/2} = 0.78$ V, $E_{onset} = 0.89$ V). To further determine the ORR path, a RRDE technology is performed to evaluate the corresponding electron transfer number n and generation of H_2O_2%. The H_2O_2% and the n for NSC-PT-0.1 are 9.38% and 3.81, indicating high four-electron path selectivity (Fig. S4d). Moreover, the excellent ORR kinetics of the NSC-PT-0.1 catalyst is confirmed by a lower Tafel slope of 123 mV·dec^{-1} compared to of the other control samples (Fig. S4e and Table S2). Figure S4f and Table S2 show that NSC-PT-0.1 has a higher C_{dl} value (68.69 mF cm^{-2}) than other control catalysts, indicating that this catalyst has larger ECSA. It is beneficial for the exposure

of active sites, promoting the transfer rate of oxygen-containing intermediates, thereby improving ORR reaction activity and kinetics [33, 44]. It can be seen that NSC-PT-0.1 possesses better ORR performance than other samples in 0.1 M KOH.

Based on the exploration of biomass with different ratios of hard-soft templates, we further study the effect of hard and soft templates. The ORR activity of catalysts is firstly explored by measuring CV in O_2-saturated 0.1 M KOH media (Fig. 3a). The ORR peak potential of NSC-PT-0.1 appears at 0.85 V, which is more positive than those of NSC-PT-0 (0.80 V), NSC-PT-Z (0.82 V), NSC-PT–S (0.83 V), and commercial Pt/C (0.82 V), indicating the higher ORR activity for NSC-PT-0.1. The ORR performances are further examined by the LSV curves at a rotation rate of 1600 rpm through using RRDE in O_2-saturated 0.1 M KOH condition (Fig. 3b and Table S2). Figure 3c shows that the E_{onset} is 0.93 V and the $E_{1/2}$ is 0.83 V for NSC-PT-0.1, which are more positive than those of NSC-PT-0 ($E_{onset} = 0.88$ V, $E_{1/2} = 0.74$ V), NSC-PT-Z ($E_{onset} = 0.90$ V, $E_{1/2} = 0.80$ V), NSC-PT–S ($E_{onset} = 0.91$ V, $E_{1/2} = 0.81$ V), and commercial Pt/C ($E_{onset} = 0.98$ V, $E_{1/2} = 0.86$ V). The fast electron transfer rate of NSC-PT-0.1 is certified by the RRDE tests (Fig. 3d). NSC-PT-0.1 reveals a high n value of 3.8–4.0 within the potential window of 0.2–0.8 V, corresponding to a low H_2O_2 yield below 9.38%, which are even superior to those of Pt/C, suggesting a four-electron ORR pathway, the Tafel slope for NSC-PT-0.1 is 123 mV dec^{-1}, lower than those of NSC-PT-0 (253 mV dec^{-1}), NSC-PT-Z (153 mV dec^{-1}), NSC-PT–S (149 mV dec^{-1}), and Pt/C (144 mV dec^{-1}), demonstrating the fastest ORR kinetics (Fig. 3e). The C_{dl} derived from electrochemical active area (ECSA) is also applied to evaluate the ORR catalytic activity by determining CV curves with different scan rates from 5 to 50 mV s^{-1} (Fig. 3f–g). The C_{dl} of NSC-PT-0.1 is 68.69 mF cm^{-2}, higher than those of NSC-PT-0 (17.95 mF cm^{-2}), NSC-PT-Z (65.42 mF cm^{-2}), NSC-PT–S (29.85 mF cm^{-2}), and Pt/C (38.31 mF cm^{-2}), confirming higher electrochemical activity area. Furthermore, the catalytic cycling stability of the ORR is crucial for evaluating the durability of catalysts. After 10,000 CV cycles, the peak potential and peak current of NSC-PT-0.1 are almost identical to the initial one, while the peak potential of Pt/C shifts negatively by 30 mV, revealing the better cycle stability for NSC-PT-0.1 (Fig. 3h). The tolerance of NSC-PT-0.1 and Pt/C toward CH_3OH was tested by injecting 3 mL 3 M
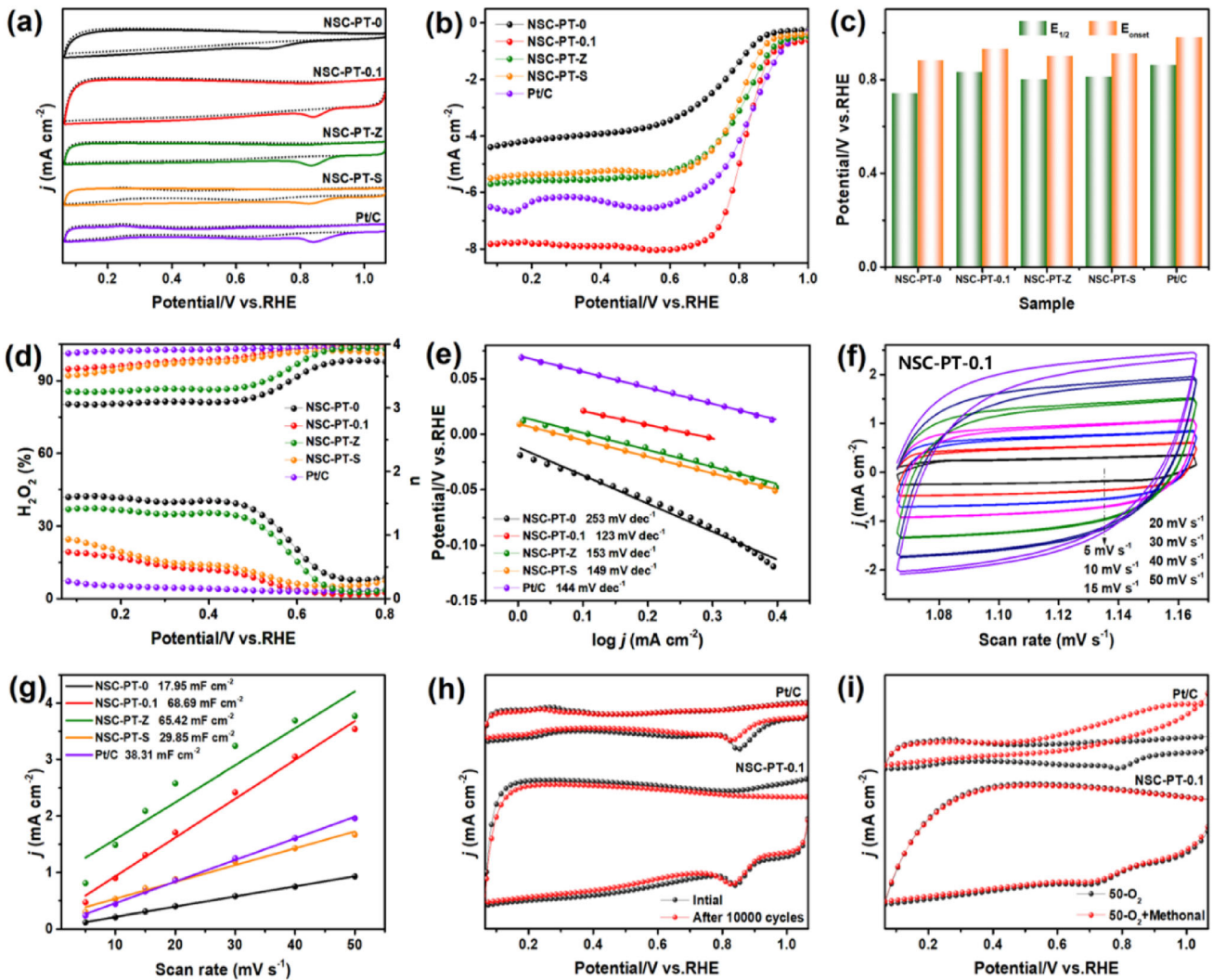
Figure 3 ORR performances in 0.1 M KOH: **a** CV curves, **b** LSV curves at 1600 rpm, **c** $E_{1/2}$ and E_{onset}, **d** $H_2O_2\%$ and *n*, **e** Tafel plots, **f** current density at different scan rates (5–50 mV s^{-1}) in the potentiostatic interval (1.07 ∼ 1.17 V), **g** C_{dl} curves, **h** stability tests, **i** methanol tolerance tests images of NSC-PT-0, NSC-PT-0.1, NSC-PT-Z, and NSC-PT–S.

methanol solution into the 30 mL 0.1 M KOH. The CV curves of NSC-PT-0.1 show an ignorable change, whereas Pt/C exhibits a typical methanol oxidation peak instead of the ORR peak (Fig. 3i). Therefore, NSC-PT-0.1 reveals high ORR activity, superior methanol tolerance, and stability in alkaline medium. It is related to the hierarchically pore structure of NSC-PT-0.1, which facilitates the exposure of active sites and mass transport [49].

Excellent ORR property of the catalysts in 0.1 M KOH media stimulates us to study the activity in 0.5 M H_2SO_4 condition. The electrocatalytic performances of samples with different ratios of the hard-soft template toward ORR are also assessed in O_2-saturated 0.5 M H_2SO_4 electrolyte. RRDE curves of

NSC-PT-*x* at the rotation rate of 1600 rpm are measured and have demonstrated that NSC-PT-0.1 has a more positive half-wave potential (Fig. S5a). Compared with the NSC-PT-0.1 catalyst, the NSC-PT-0.04, NSC-PT-0.07, NSC-PT-0.5, and NSC-PT-1 controls exhibit apparently worse ORR activity, such as the lower $E_{1/2}$ (0.52 V, 0.64 V, 0.60 V, and 0.61 V, respectively) (Fig. S5b). The n and $H_2O_2\%$ of these catalysts are determined at potentials from 0.2 to 0.8 V by RRDE measurement (Fig. S5c). The average $H_2O_2\%$ yield and n value of NSC-PT-0.1 are calculated to be 2.16% and 3.96, which are better than those of NSC-PT-0.04 ($H_2O_2\% = 7.57\%$, $n = 3.85$), NSC-PT-0.07 ($H_2O_2\% = 3.56\%$, $n = 3.92$), NSC-PT-0.5 ($H_2O_2\% = 2.75\%$, $n = 3.94$), and NSC-PT-1

(H_2O_2% = 4.98%, n = 3.90), suggesting an effective 4-electron process. It can be seen that NSC-PT-0.1 possesses prominent ORR performance in 0.5 M H_2SO_4.

Next, in order to study the effect of hard and soft templates, the electrocatalytic performances of the catalysts toward ORR are also assessed in O_2-saturated 0.5 M H_2SO_4 electrolyte. As shown in Fig. 4a and Table S3, the obvious reduction peaks, observed in CV curves under O_2-saturated media, elucidate the ORR catalytic activity for prepared samples and Pt/C catalysts. The cathodic peak potential of NSC-PT-0.1 (0.84 V) is much more positive than those of NSC-PT-0 (0.52 V), NSC-PT-Z (0.68 V), NSC-PT–S (0.60 V), and Pt/C (0.81 V), indicating the excellent ORR activity. Figure 4b and Table S3 show the LSV polarization plots of the as-prepared catalysts and 20 wt% Pt/C. As shown in Fig. 4c, NSC-PT-0.1 delivers a more positive onset potential of 0.80 V and half-wave potential of 0.69 V than those of NSC-PT-0 (E_{onset} = 0.74 V, $E_{1/2}$ = 0.43 V), NSC-PT-Z (E_{onset} = 0.79 V, $E_{1/2}$ = 0.60 V), NSC-PT–S (E_{onset} = 0.80 V, $E_{1/2}$ = 0.50 V), and comparable to Pt/C (E_{onset} = 0.91 V, $E_{1/2}$ = 0.76 V). The average H_2O_2% yield and n value of NSC-PT-0.1 are calculated to be 2.16% and 3.96,

which is better than those of NSC-PT-0 (H_2O_2% = 17.30%, n = 3.65), NSC-PT-Z (H_2O_2% = 3.66%, n = 3.93), NSC-PT-S (H_2O_2% = 4.48%, n = 3.91), and Pt/C (H_2O_2% = 7.98%, n = 3.84), suggesting an effective 4-electron process (Fig. 4d). Excellent durability and methanol tolerance are also crucial for ORR electrocatalysts. As depicted in Fig. 4e, after 5000 continuous CV cycles, the peak potential of NSC-PT-0.1 is almost identical to the original one, much better than that of Pt/C. Additionally, the resistance of methanol crossover has been tested by injecting 3 mL 3 M methanol into the electrolyte during the CV test. As shown in Fig. 4f, the obvious methanol poisoning effect containing a distinct methanol redox peak and a significant current drop is observed for Pt/C, whereas the current response of NSC-PT-0.1 barely decays upon the addition of CH_3OH. The consequence demonstrates that NSC-PT-0.1 exhibits more excellent tolerance to methanol than Pt/C catalyst. By making a preliminary summary, NSC-PT-0.1 possesses superior stability and selectivity toward ORR in 0.1 M KOH electrolyte, which can be regarded as a promising electrocatalyst for practical application [50, 51].
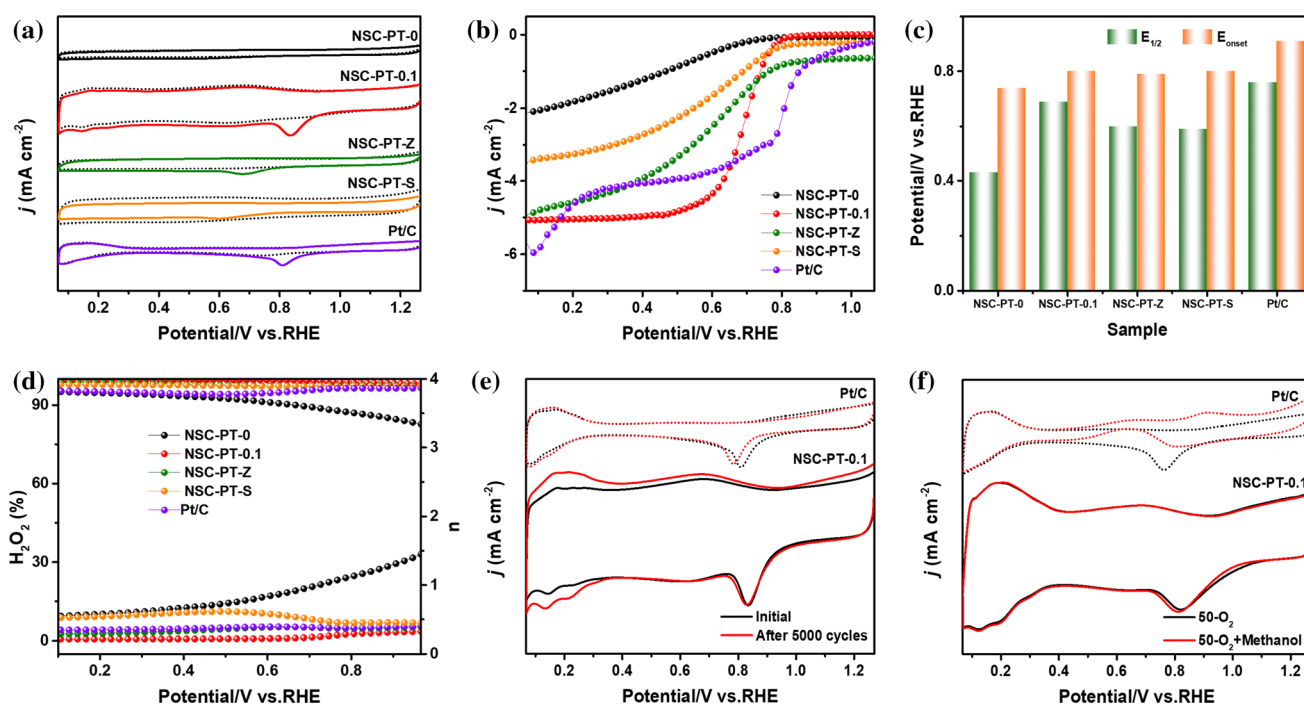

Figure 4 ORR performances in 0.5 M H_2SO_4: **a** CV curves, **b** LSV curves at 1600 rpm, **c** $E_{1/2}$ and E_{onset}, **d** H_2O_2% and n, **e** stability tests, **f** methanol tolerance tests images of NSC-PT-0, NSC-PT-0.1, NSC-PT-Z, and NSC-PT–S.

Universality study of other biomass-derived catalysts

To prove the versatility of the hard-soft template strategy, the optimal dosages of hard and soft templates have been selected to prepare other biomass-derived carbon materials (NSC-CL-0/0.1, NSC-WS-0/0.1, and NSC-GL-0/0.1). Figure 5a–c displays the SEM images of three different hierarchical N, S co-doped carbon materials (NSC-CL-0.1, NSC-WS-0.1, and NSC-GL-0.1) derived from the Carrot, Whorled stonecrop, and Ginkgo leaf. It is worth noting that they all possess the similar hierarchical structures to the NSC-PT-0.1. Moreover, structural characteristics were further confirmed by XRD and Raman patterns (Fig. S6). XRD patterns of these catalysts show the diffraction peaks at around 23° and 44° assigned to

the (002) and (101) crystal planes of graphitic carbon, similar to the patterns of NSC-CL-0, NSC-WS-0, and NSC-GL-0 [52]. Additionally, the Raman spectra confirm that the higher I_D/I_G values are achieved for NSC-CL-0.1 (1.14), NSC-WS-0.1 (1.13), and NSC-GL-0.1 (1.13) than those of NSC-CL-0 (1.03), NSC-WS-0 (1.07), and NSC-GL-0 (1.10), implying the existence of richer defects (Table S4). To further confirm the effect of templating agents on pore structure, N_2 adsorption/desorption isotherms and pore size distribution tests were also performed for the samples, as shown in Fig. 5d, e. NSC-CL-0/0.1, NSC-WS-0/0.1, and NSC-GL-0/0.1 have type-IV isotherms. It is calculated that the S_{BET}, V_{Total}, and $V_{Average}$ have a significant increase with the addition of the hard-soft template agent. The pore structures are similar to
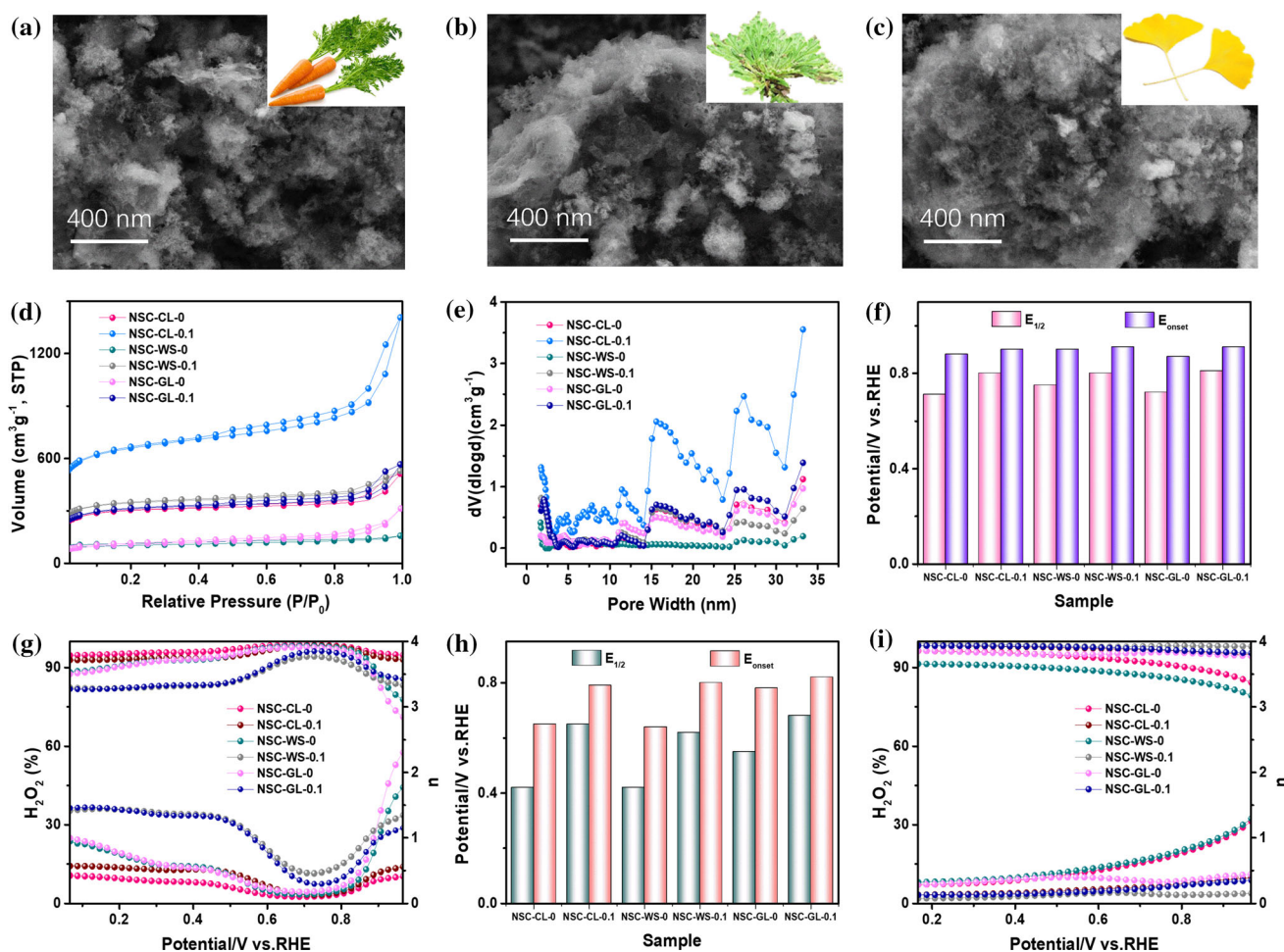

Figure 5 SEM images of NSC-CL-0.1 (**a**, the insert is Carrot), NSC-WS-0.1 (**b**, the insert is Whorled stonecrop), NSC-GL-0.1 (**c**, the insert is Ginkgo leaf); N_2 adsorption/desorption isotherms **d**, and pore size distribution curves **e**, $E_{1/2}$ and E_{onset}, $H_2O_2\%$ and n in 0.1 M KOH (**f**, **g**), $E_{1/2}$ and E_{onset}, $H_2O_2\%$ and n in 0.5 M H_2SO_4 **h**, **i** images of NSC-CL, NSC-WS, NSC-GL series of catalysts.

those of NSC-PT-0.1, revealing the universality of the hard-soft template strategy.

As the electrochemical performance of catalysts relies on mesopore-dominated hierarchical porous structure and the amount of catalytically active sites, we further investigate the ORR activity of various carbon-based materials derived from different biomasses, including the NSC-CL-0.1, NSC-WS-0.1, and NSC-GL-0.1. In terms of $E_{1/2}$ in 0.1 M KOH media and 0.5 M H_2SO_4 media, the ORR activity of NSC-CL-0.1 (0.80 V, 0.65 V), NSC-WS-0.1 (0.80 V, 0.62 V), and NSC-GL-0.1 (0.81 V, 0.68 V) is much higher than those of NSC-CL-0 (0.71 V, 0.42 V), NSC-WS-0 (0.75 V, 0.42 V), and NSC-GL-0 (0.72 V, 0.55 V). To further determine the ORR path, a RRDE technology is also performed to evaluate the n and generation of $H_2O_2\%$. A low HO_2^- (in 0.1 M KOH) or H_2O_2 (in 0.5 M H_2SO_4) yield (< 10%), and an electron transfer number n for NSC-CL-0.1, NSC-WS-0.1 and NSC-GL-0.1 approaching four are determined at potentials from 0.2 to 0.8 V, indicating high four-electron path selectivity (Fig. S4d, 5c). Figure S4f and Table S2 show NSC-CL-0.1, NSC-WS-0.1, and NSC-GL-0.1 have a higher C_{dl} value (47.84, 65.40, and 56.33 mF cm^{-2}) than other NSC-CL-0 (18.51 mF cm^{-2}), NSC-WS-0 (13.92 mF cm^{-2}), and NSC-GL-0 (22.07 mF cm^{-2}) catalysts, indicating the larger ECSA in 0.1 M KOH. The hard-soft templates are beneficial for providing more active sites and promoting the transfer rate of oxygen-containing intermediates, thereby improving ORR reaction activity and kinetics [53]. It can be seen that NSC-CL-0.1, NSC-WS-0.1, and NSC-GL-0.1 possess better ORR activity than other control samples in 0.1 M KOH and 0.5 M H_2SO_4 media. In summary, the hard-soft template method can not only promote the exposion of active sites but also generate more edge and defect sites, enabling the synthesized carbon-based catalysts with excellent ORR activity [54, 55].

Zn-air battery performance

To evaluate the practical application of NSC-PT-0.1 catalyst, a ZAB was assembled through adopting carbon paper-supported NSC-PT-0.1 catalyst (2 mg cm^{-2}) as the air cathode, Zn foil as the anode, and 6.0 M KOH with 0.2 M $Zn(Ac)_2$ as the electrolyte (Fig. 6a). The ZAB with commercial Pt/C as cathode catalyst was also assembled. The NSC-PT-0.1-based ZAB exhibits a peak power density of 155.55 mW

cm^{-2}, which is significantly higher than that of the Pt/C-based ZAB (137.49 mW cm^{-2}) (Fig. 6b). In the charge–discharge polarization curves, the NSC-PT-0.1-based ZAB has a lower charge–discharge gap of 0.87 V at a current density of 20 mA cm^{-2} than that of the Pt/C-based ZAB (1.09 V) (Fig. 6c). As displayed in Fig. 6d, the discharge curves of NSC-PT-0.1-based ZAB possess higher values than that of Pt/C-based ZAB at a series of current densities (1 ∼ 100 mA cm^{-2}). It is attributed to the mesopore-dominated hierarchically porous structure and heteroatoms-doped of NSC-PT-0.1, which provides effective mass transfer channels for the diffusion of O_2 and electrolytes [56–58]. As a result, the discharge voltage resumes reversibly once the current density reduces to 1 mA cm^{-2}, indicating the superior rate performance. The battery driven by NSC-PT-0.1 catalyst exhibits a stable open-circuit voltage (1.46 V) superior to Pt/C-based ZAB (1.44 V) in Fig. 6e. Remarkably, three series-connected NSC-PT-0.1-based ZABs can successfully power a 3.7 V light-emitting diode (LED) screen (Fig. 6f) or a 3.0 V electronic toy (**Movie SI**), demonstrating the feasible application of NSC-PT-0.1 catalyst. Besides, the cycle stability of ZAB with NSC-PT-0.1 catalyst was also evaluated by continuous galvanostatic discharge–charge test at 2 mA cm^{-2}. The NSC-PT-0.1-based ZAB can repeatedly cycle at 2 mA cm^{-2} for a total of 216 h in Fig. 6g. Compared to a Pt/C-based ZAB, a slightly lower initial charge–discharge voltage gap is observed for the NSC-PT-0.1-based ZAB, indicating a better rechargeability (Fig. 6h). After about 102 h, the NSC-PT-0.1-based ZAB shows a negligible voltage change, whereas Pt/C demonstrates a significantly increase in the voltage gap under the same condition, demonstrating superior stability of the NSC-PT-0.1-based ZAB. The above results verify the promising potential of NSC-PT-0.1 as a high-efficiency and durable catalyst for ZABs [59].

Conclusions

In summary, a feasible hard-soft (SiO_2–$ZnCl_2$) template strategy has been developed to construct mesopore-dominated porous heteroatom-doped carbon materials from various biomass precursors (Pointed tail, Carrot, Whorled stonecrop, and Ginkgo leaf). The employed SiO_2 and $ZnCl_2$ templates result in the optimized mesopore-dominated hierarchical
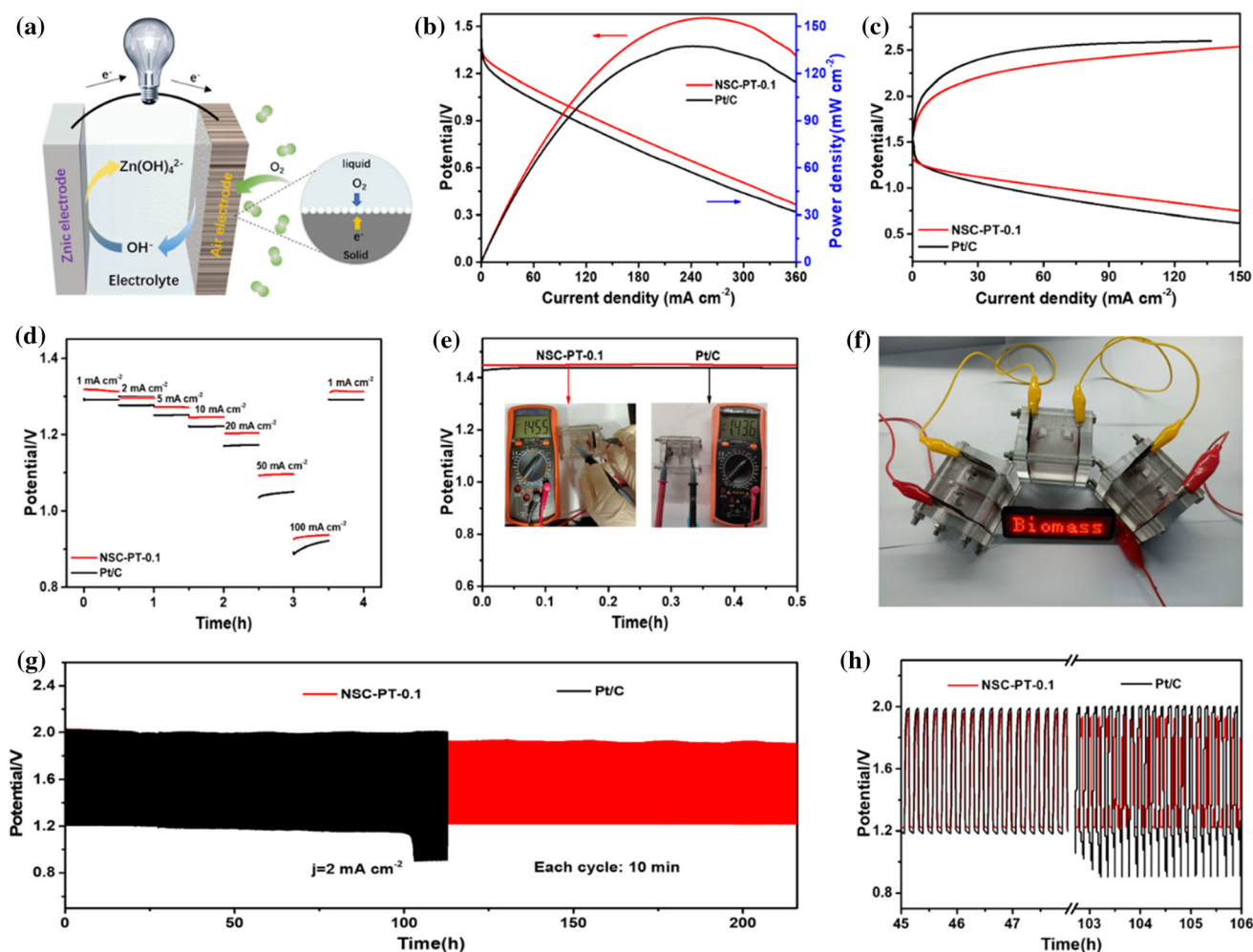
Figure 6 a Schematic diagram of ZAB with NSC-PT-0.1 as the air cathode. **b** Discharge polarization curves and power density curves of NSC-PT-0.1-based and Pt/C-based ZABs. **c** Charge and discharge polarization curves. **d** Discharge curves at different current densities from 1 to 100 mA cm^{-2}. **e** Open-circuit voltage. **f** Photographs of the LED screen powered by three series of NSC-PT-0.1-based ZABs. **g**–**h** Long-term discharge–charge cycling stability curves at 2 mA cm.$^{-2}$.

porous carbon material (NSC-PT-0.1) with large S_{BET} of 2357.55 m^2 g^{-1} and high N, S content of 2.32 at.%. The unique structure not only promotes the exposion of assessable active sites, but also increases the contact wettability of catalyst and electrolyte, improving the transmission efficiency of O$_2$ and ions. Therefore, NSC-PT-0.1 exhibits excellent alkaline (E_{onset} = 0.93 V, $E_{1/2}$ = 0.82 V, and j_L = 7.84 mA cm^{-2}) and acidic (E_{onset} = 0.80 V, $E_{1/2}$ = 0.69 V, and j_L = 5.08 mA cm^{-2}) ORR catalytic activity, long-term stability (alkaline 10,000 CV cycles and acidic 5000 CV cycles), and methanol tolerance. Furthermore, when NSC-PT-0.1 is employed as a catalytic layer of air electrode, the assembled ZAB exhibits a better discharge power output capability (155.55 mW cm^{-2}) and long-term cycle stability (216 h) than Pt/C-based

ZAB. Besides, the Carrot, Whorled stonecrop, and Ginkgo leaf have been simultaneously chosen to confirm the versatility of the hard-soft template method. This work provides a promising approach for synthesizing low-cost, efficient, and stable ORR electrocatalyst for ZABs through the high-quality utilization of biomass resources.

Declarations

Conflict of interest The authors declare no conflict of interest in this paper.

Supplementary Information: The online version contains supplementary material available at https://doi.org/10.1007/s10853-022-07784-7.

References

[1] Li H, Di S, Niu P, Wang S, Wang J, Li L (2022) A durable half-metallic diatomic catalyst for efficient oxygen reduction. Energy Environ Sci 15:1601. https://doi.org/10.1039/D1EE03194E

[2] Yang G, Zhu J, Yuan P et al (2021) Regulating Fe-spin state by atomically dispersed Mn–N in Fe–N–C catalysts with high oxygen reduction activity. Nat Commun 12:1734. https://doi.org/10.1038/s41467-021-21919-5

[3] Chen C, Sun Z, Li Y, Yi L, Hu H (2021) Retraction Note to: Self-assembly of N doped 3D porous carbon frameworks from carbon quantum dots and its application for oxygen reduction reaction. J Mater Sci-Mater Electron 32:12743. https://doi.org/10.1007/s10854-021-05873-y

[4] Lim J, Jung J-W, Kim N-Y et al (2020) N_2-dopant of graphene with electrochemically switchable bifunctional ORR/OER catalysis for Zn-air battery. Energy Storage Mater 32:517. https://doi.org/10.1016/j.ensm.2020.06.034

[5] Chen C, Sun Z, Li Y, Yi L, Hu H (2021) Retraction Note to: self-assembly of N doped 3D porous carbon frameworks from carbon quantum dots and its application for oxygen reduction reaction. J Mater Sci Mater Electron 32:12743. https://doi.org/10.1007/s10854-021-05873-y

[6] Liu H, Liu Y, Mehdi S et al (2021) Surface phosphorus-induced CoO coupling to monolithic carbon for efficient air electrode of quasi-solid-state Zn–air batteries. Adv Sci 8:2101314. https://doi.org/10.1002/advs.202101314

[7] Fritz KE, Yan Y, Suntivich J (2020) Erratum to: Influence of 3d transition-metal substitution on the oxygen reduction reaction electrocatalysis of ternary nitrides in acid. Nano Res 13:2578. https://doi.org/10.1007/s12274-020-2939-x

[8] Bi Z, Kong Q, Cao Y et al (2019) Biomass-derived porous carbon materials with different dimensions for supercapacitor electrodes: a review. J Mater Chem A 7:16028. https://doi.org/10.1039/C9TA04436A

[9] Li W, Zhou M, Li H, Wang K, Cheng S, Jiang K (2015) A high performance sulfur-doped disordered carbon anode for sodium ion batteries. Energy Environ Sci 8:2916. https://doi.org/10.1039/C5EE01985K

[10] Ait El Fakir A, Anfar Z, Enneiymy M, Jada A, El Alem N (2022) New insights into N, S doped carbon from conjugated polymers for efficient persulfate activation: Role of hydrogel beads in enhancement of stability. Chem Eng J 442:136055. https://doi.org/10.1016/j.cej.2022.136055

[11] Yan T, Yang L, Dai W et al (2018) On the deactivation mechanism of zeolite catalyst in ethanol to butadiene conversion. J Catal 367:7. https://doi.org/10.1016/j.jcat.2018.08.019

[12] Gao S, Li X, Li L, Wei X (2017) A versatile biomass derived carbon material for oxygen reduction reaction, supercapacitors and oil/water separation. Nano Energy 33:334. https://doi.org/10.1016/j.nanoen.2017.01.045

[13] Tian M, Zhang D, Wang M et al (2020) Engineering flexible 3D printed triboelectric nanogenerator to self-power electro-Fenton degradation of pollutants. Nano Energy 74:104908. https://doi.org/10.1016/j.nanoen.2020.104908

[14] Liu X, Li X, Zhao X, Gao Y, Cao Z, Liu J (2022) WS_2@-Co_9S_8@N/C core–shell as multifunctional electrocatalysts for dye-sensitized solar cell, oxygen reduction reaction and oxygen evolution reaction. J Mater Sci 57:6293. https://doi.org/10.1007/s10853-022-07028-8

[15] Nzediegwu C, Naeth MA, Chang SX (2022) Feedstock type drives surface property, demineralization and element leaching of nitric acid-activated biochars more than pyrolysis temperature. Bioresour Technol 344:126316. https://doi.org/10.1016/j.biortech.2021.126316

[16] Li S, Han K, Li J, Li M, Lu C (2017) Preparation and characterization of super activated carbon produced from gulfweed by KOH activation. Microporous Mesoporous Mater 243:291. https://doi.org/10.1016/j.micromeso.2017.02.052

[17] Zhao Z, Hao S, Hao P et al (2015) Lignosulphonate-cellulose derived porous activated carbon for supercapacitor electrode. J Mater Chem A 3:15049. https://doi.org/10.1039/C5TA02770E

[18] Hui TS, Zaini MAA (2015) Potassium hydroxide activation of activated carbon: a commentary. Carbon Lett 16:275. https://doi.org/10.5714/cl.2015.16.4.275

[19] Kim M-J, Choi SW, Kim H, Mun S, Lee KB (2020) Simple synthesis of spent coffee ground-based microporous carbons using K_2CO_3 as an activation agent and their application to CO_2 capture. Chem Eng J. https://doi.org/10.1016/j.cej.2020.125404

[20] Zhao Y, Li X, Jia X, Gao S (2019) Why and how to tailor the vertical coordinate of pore size distribution to construct

ORR-active carbon materials? Nano Energy 58:384. https://doi.org/10.1016/j.nanoen.2019.01.057

[21] Li X, Zhao Y, Yang Y, Gao S (2019) A universal strategy for carbon–based ORR–active electrocatalyst: one porogen, two pore–creating mechanisms, three pore types. Nano Energy 62:628. https://doi.org/10.1016/j.nanoen.2019.05.066

[22] Astafan A, Benghalem MA, Pouilloux Y et al (2016) Particular properties of the coke formed on nano-sponge *BEA zeolite during ethanol-to-hydrocarbons transformation. J Catal 336:1. https://doi.org/10.1016/j.jcat.2016.01.002

[23] Ashraf MA, Liu Z, Zhang D, Najafi M (2020) Aluminum-doped silicon nanocage and boron-doped carbon nanocage as catalysts to oxygen reduction reaction (ORR): a computational investigation. Ionics 26:3085. https://doi.org/10.1007/s11581-020-03450-7

[24] Liu M, Zhu F, Cao W et al (2022) Multifunctional sulfate-assistant synthesis of seaweed-like N, S-doped carbons as high-performance anodes for K-ion capacitors. J Mater Chem A. https://doi.org/10.1039/D2TA01431A

[25] Yang G, Wang L, Jiang H (2021) Preparation of β zeolite with intracrystalline mesoporosity via surfactant -templating strategy and its application in ethanol-acetaldehyde to butadiene. Microporous Mesoporous Mater 316:110949. https://doi.org/10.1016/j.micromeso.2021.110949

[26] Zhang M, Qin Y, Jiang H, Wang L (2021) Protective desilication of β zeolite: A mechanism study and its application in ethanol-acetaldehyde to 1,3-butadiene. Microporous Mesoporous Mater 326:111359. https://doi.org/10.1016/j.micromeso.2021.111359

[27] Fan L, Yang L, Ni X, Han J, Guo R, Zhang C (2016) Nitrogen-enriched meso-macroporous carbon fiber network as a binder-free flexible electrode for supercapacitors. Carbon 107:629. https://doi.org/10.1016/j.carbon.2016.06.067

[28] Wan X, Liu X, Li Y et al (2019) Fe–N–C electrocatalyst with dense active sites and efficient mass transport for high-performance proton exchange membrane fuel cells. Nat Catal 2:259. https://doi.org/10.1038/s41929-019-0237-3

[29] Mendoza R, Oliva J, Rodriguez-Gonzalez V (2022) Effect of the micro-, meso- and macropores on the electrochemical performance of supercapacitors: a review. Int J Energy Res 46:6989. https://doi.org/10.1002/er.7670

[30] Li X, Guan BY, Gao S, Lou XW (2019) A general dual-templating approach to biomass-derived hierarchically porous heteroatom-doped carbon materials for enhanced electrocatalytic oxygen reduction. Energy Environ Sci 12:648. https://doi.org/10.1039/C8EE02779J

[31] Dolas H, Sahin O, Saka C, Demir H (2011) A new method on producing high surface area activated carbon: the effect of salt on the surface area and the pore size distribution of activated carbon prepared from pistachio shell. Chem Eng J 166:191. https://doi.org/10.1016/j.cej.2010.10.061

[32] Hussein MAT, Motawea MM, Elsenety MM, El-Bahy SM, Gomaa H (2022) Mesoporous spongy Ni–Co oxides@wheat straw-derived SiO_2 for adsorption and photocatalytic degradation of methylene blue pollutants. Appl Nanosci. https://doi.org/10.1007/s13204-021-02318-0

[33] Zhang W, Chen Y-P, Zhang L, Feng J-J, Li X-S, Wang A-J (2022) Theophylline-regulated pyrolysis synthesis of nitrogen-doped carbon nanotubes with iron-cobalt nanoparticles for greatly boosting oxygen reduction reaction. J Colloid Interface Sci 626:653. https://doi.org/10.1016/j.jcis.2022.06.130

[34] Ma Q, Jin H, Zhu J et al (2021) Stabilizing Fe–N–C catalysts as model for oxygen reduction reaction. Adv Sci 8:2102209. https://doi.org/10.1002/advs.202102209

[35] Sharma S, Basu S, Shetti NP, Mondal K, Sharma A, Aminabhavi TM (2022) Versatile graphitized carbon nanofibers in energy applications. ACS Sustain Chem Eng 10:1334. https://doi.org/10.1021/acssuschemeng.1c06762

[36] Cui L, Cui L, Li Z et al (2019) A copper single-atom catalyst towards efficient and durable oxygen reduction for fuel cells. J Mater Chem A 7:16690. https://doi.org/10.1039/C9TA03518D

[37] Yu H, Shang L, Bian T et al (2016) Nitrogen-doped porous carbon nanosheets templated from g-C_3N_4 as metal-free electrocatalysts for efficient oxygen reduction reaction. Adv Mater 28:5080. https://doi.org/10.1002/adma.201600398

[38] Raveendran K, Ganesh A, Khilar KC (1996) Pyrolysis characteristics of biomass and biomass components. Fuel 75:987. https://doi.org/10.1016/0016-2361(96)00030-0

[39] Wei X, Li H, Ce Yuan Q, Li SC (2009) Preparation of nano-ZnO supported on porous carbon and the growth mechanism. Microporous Mesoporous Mater 118:307. https://doi.org/10.1016/j.micromeso.2008.09.008

[40] Taheri E, Fatehizadeh A, Lima EC, Rezakazemi M (2022) High surface area acid-treated biochar from pomegranate husk for 2, 4-dichlorophenol adsorption from aqueous solution. Chemosphere 295:133850. https://doi.org/10.1016/j.chemosphere.2022.133850

[41] Xu D, Tong Y, Yan T, Shi L, Zhang D (2017) N, P-codoped meso-/microporous carbon derived from biomass materials via a dual-activation strategy as high-performance electrodes for deionization capacitors. ACS Sustainable Chem Eng 5:5810. https://doi.org/10.1021/acssuschemeng.7b00551

[42] Men B, Sun Y, Li M et al (2016) Hierarchical metal-free nitrogen-doped porous graphene/carbon composites as an efficient oxygen reduction reaction catalyst. ACS Appl Mater Interfaces 8:1415. https://doi.org/10.1021/acsami.5b10642

[43] Wang S, Qin J, Meng T, Cao M (2017) Metal-organic framework-induced construction of actiniae-like carbon nanotube assembly as advanced multifunctional electrocatalysts for overall water splitting and Zn-air batteries. Nano Energy 39:626. https://doi.org/10.1016/j.nanoen.2017.07.043

[44] Yan Q, Sun R-M, Wang L-P, Feng J-J, Zhang L, Wang A-J (2021) Cobalt nanoparticles/ nitrogen, sulfur-codoped ultra-thin carbon nanotubes derived from metal organic frameworks as high-efficiency electrocatalyst for robust rechargeable zinc-air battery. J Colloid Interface Sci 603:559. https://doi.org/10.1016/j.jcis.2021.06.133

[45] Ren J-T, Yuan Z-Y (2019) Bifunctional electrocatalysts of cobalt sulfide nanocrystals in situ decorated on N, S-codoped porous carbon sheets for highly efficient oxygen electrochemistry. ACS Sustain Chem Eng 7:10121. https://doi.org/10.1021/acssuschemeng.9b01699

[46] Xue X, Yang H, Yang T et al (2019) N, P-coordinated fullerene-like carbon nanostructures with dual active centers toward highly-efficient multi-functional electrocatalysis for CO2RR, ORR and Zn-air battery. J Mater Chem A 7:15271. https://doi.org/10.1039/C9TA03828K

[47] Zhang J, Zhang J, He F et al (2021) Defect and doping co-engineered non-metal nanocarbon ORR electrocatalyst. Nano-Micro Lett 13:65. https://doi.org/10.1007/s40820-020-00579-y

[48] Li L, Yang H, Miao J et al (2017) Unraveling oxygen evolution reaction on carbon-based electrocatalysts: effect of oxygen doping on adsorption of oxygenated intermediates. ACS Energy Lett 2:294. https://doi.org/10.1021/acsenergylett.6b00681

[49] Fan X-Z, Du X, Pang Q-Q, Zhang S, Liu Z-Y, Yue X-Z (2022) In situ construction of bifunctional N-doped carbon-anchored Co nanoparticles for OER and ORR. ACS Appl Mater Interfaces 14:8549. https://doi.org/10.1021/acsami.1c21445

[50] He Y, Yang X, Li Y et al (2022) Atomically dispersed Fe-Co dual metal sites as bifunctional oxygen electrocatalysts for rechargeable and flexible zn-air batteries. ACS Catal 12:1216. https://doi.org/10.1021/acscatal.1c04550

[51] Liu Z, Wan J, Li M, Shi Z, Liu J, Tang Y (2022) Synthesis of Co/CeO_2 hetero-particles with abundant oxygen-vacancies supported by carbon aerogels for ORR and OER. Nanoscale 14:1997. https://doi.org/10.1039/D1NR07595K

[52] Wang B, Tang J, Zhang X et al (2022) Nitrogen doped porous carbon polyhedral supported Fe and Ni dual-metal single-atomic catalysts: template-free and metal ligand-free sysnthesis with microwave-assistance and d-band center modulating for boosted ORR catalysisin zinc-air batteries. Chem Eng J. https://doi.org/10.1016/j.cej.2022.135295

[53] Cai W, Zhang Y, Jia Y, Yan J (2020) Flexible heteroatom-doped porous carbon nanofiber cages for electrode scaffolds. Carbon Energy 2:472. https://doi.org/10.1002/cey2.46

[54] Zhao M, Liu H, Zhang H et al (2021) A pH-universal ORR catalyst with single-atom iron sites derived from a double-layer MOF for superior flexible quasi-solid-state rechargeable Zn–air batteries. Energy Environ Sci 14:6455. https://doi.org/10.1039/D1EE01602D

[55] Zhao Y, Liu Y, Chen Y, Liu X, Li X, Gao S (2021) A treasure map for nonmetallic catalysts: optimal nitrogen and fluorine distribution of biomass-derived carbon materials for high-performance oxygen reduction catalysts. J Mater Chem A 9:18251. https://doi.org/10.1039/d1ta05485f

[56] Han Z, Feng J-J, Yao Y-Q, Wang Z-G, Zhang L, Wang A-J (2021) Mn, N, P-tridoped bamboo-like carbon nanotubes decorated with ultrafine Co2P/FeCo nanoparticles as bifunctional oxygen electrocatalyst for long-term rechargeable Zn-air battery. J Colloid Interface Sci 590:330. https://doi.org/10.1016/j.jcis.2021.01.053

[57] Chen Y-P, Lin S-Y, Sun R-M et al (2022) FeCo/FeCoP encapsulated in N, Mn-codoped three-dimensional fluffy porous carbon nanostructures as highly efficient bifunctional electrocatalyst with multi-components synergistic catalysis for ultra-stable rechargeable Zn-air batteries. J Colloid Interface Sci 605:451. https://doi.org/10.1016/j.jcis.2021.07.082

[58] Sun R-M, Zhang L, Feng J-J, Fang K-M, Wang A-J (2022) In situ produced Co9S8 nanoclusters/Co/Mn-S, N multi-doped 3D porous carbon derived from eriochrome black T as an effective bifunctional oxygen electrocatalyst for rechargeable Zn-air batteries. J Colloid Interface Sci 608:2100. https://doi.org/10.1016/j.jcis.2021.10.144

[59] Gao S, Yang H, Rao D et al (2022) Supercritical CO_2 assisted synthesis of highly accessible iron single atoms and clusters on nitrogen-doped carbon as efficient oxygen reduction electrocatalysts. Chem Eng J 433:134460. https://doi.org/10.1016/j.cej.2021.134460